

# Gas flow in barred potentials

Mattia C. Sormani, James Binney, John Magorrian

▶ **To cite this version:**

Mattia C. Sormani, James Binney, John Magorrian. Gas flow in barred potentials. Monthly Notices of the Royal Astronomical Society, 2015, 449, pp.2421-2435. 10.1093/mnras/stv441 . insu-03644947

**HAL Id: insu-03644947**
**https://insu.hal.science/insu-03644947**

Submitted on 26 Apr 2022

**HAL** is a multi-disciplinary open access archive for the deposit and dissemination of scientific research documents, whether they are published or not. The documents may come from teaching and research institutions in France or abroad, or from public or private research centers.

L'archive ouverte pluridisciplinaire **HAL**, est destinée au dépôt et à la diffusion de documents scientifiques de niveau recherche, publiés ou non, émanant des établissements d'enseignement et de recherche français ou étrangers, des laboratoires publics ou privés.

Monthly Notices
of the
ROYAL ASTRONOMICAL SOCIETY

MNRAS **449,** 2421–2435 (2015) doi:10.1093/mnras/stv441

# Gas flow in barred potentials

Mattia C. Sormani,[1⋆] James Binney[1] and John Magorrian[1,2]

[1]*Rudolf Peierls Centre for Theoretical Physics, 1 Keble Road, Oxford OX1 3NP, UK*
[2]*Institut d'Astrophysique de Paris, 98bis boulevard Arago, F-75014 Paris, France*

Accepted 2015 February 25. Received 2015 February 12; in original form 2015 January 1

**ABSTRACT**

We use a Cartesian grid to simulate the flow of gas in a barred Galactic potential and investigate the effects of varying the sound speed in the gas and the resolution of the grid. For all sound speeds and resolutions, streamlines closely follow closed orbits at large and small radii. At intermediate radii shocks arise and the streamlines shift between two families of closed orbits. The point at which the shocks appear and the streamlines shift between orbit families depends strongly on sound speed and resolution. For sufficiently large values of these two parameters, the transfer happens at the cusped orbit as hypothesized by Binney et al. over two decades ago. For sufficiently high resolutions, the flow downstream of the shocks becomes unsteady. If this unsteadiness is physical, as appears to be the case, it provides a promising explanation for the asymmetry in the observed distribution of CO.

**Key words:** ISM: kinematics and dynamics – Galaxy: kinematics and dynamics.

## 1 INTRODUCTION

More than 20 yr ago, (Binney et al. 1991, hereafter BGSBU) proposed a consistent picture to explain spectral line emission by different species, H I, CO and CS, in the Galactic-centre region $|l| < 10^\circ$ and $|b| < 2^\circ$. They related the flow of gas in an externally imposed, rigidly rotating barred potential to the structure of the longitude–velocity, $(l, v)$, plane that one obtains by projecting closed orbits along lines of sight through the disc. According to BGSBU, gas in the outer parts of the bar drifts slowly towards the centre while following $x_1$ orbits. These orbits become more and more elongated as the centre is approached, and eventually the 'cusped orbit' is reached, which has a cusp at each end. Interior to the cusped orbit, the orbits of the $x_1$ family are self-intersecting. BGSBU hypothesized that when gas reaches the cusped orbit, it encounters a shock, and then quickly plunges on to $x_2$ orbits. Thereafter, the gas drifts towards the centre following $x_2$ orbits. Using this simple representation of the gas flow, BGSBU provided an appealing interpretation of observational data: H I emission comes mainly from gas on non-self-intersecting $x_1$ orbits, CO forms as gas is shocked on reaching the cusped orbit, which explained the characteristic parallelogram-shaped envelope of CO emission in the $(l, v)$ plane, and CS emission comes from dense, post-shocked gas flowing on $x_2$ orbits.

The BGSBU picture has enjoyed considerable success and, alongside the photometric study of Blitz & Spergel (1991), convinced the community that our Galaxy is barred. In the following years, the presence of the bar has been confirmed by further photometric evidence (Stanek et al. 1994; Dwek et al. 1995; Binney, Gerhard & Spergel 1997), and there is now little doubt that the Milky Way is indeed barred.

The BGSBU picture relied on the assumption that gas streamlines follow closed orbits and that the $x_1 \rightarrow x_2$ transfer happens at the cusped orbit, and needed validation by hydro simulations. In support of their model, BGSBU pointed to simulations by Athanassoula (1992b). However, these simulations used a different potential from BGSBU, so a natural next step was to run hydro simulations in the potential BGSBU had used. One such study appeared (Jenkins & Binney 1994), but its results were not encouraging; in this simulation, orbits near the cusped $x_1$ orbit, which played a crucial role in BGSBU picture, were found to be unoccupied by gas.

More recently, numerous hydrodynamical simulations have been run with the goal of understanding the kinematics and dynamics of the cold gas in our Galaxy (Mulder & Liem 1986; Englmaier & Gerhard 1999; Fux 1999; Lee et al. 1999; Weiner & Sellwood 1999; Bissantz, Englmaier & Gerhard 2003; Rodriguez-Fernandez & Combes 2008; Baba, Saitoh & Wada 2010; Pettitt, Dobbs, Acreman & Price 2014). However, none of these simulations use the potential BGSBU used. Some used a potential inferred from infrared photometric data (Englmaier & Gerhard 1999; Bissantz et al. 2003; Rodriguez-Fernandez & Combes 2008), while others (Fux 1999) used the potential generated by a combined hydro and $N$-body simulation of the Milky Way. Notwithstanding these efforts, the interpretation of the observational data remains problematic in some aspects (Sormani & Magorrian 2015).

Most authors of papers using hydro simulations mention closed orbits, in a more or less explicit connection with BGSBU, but the literature lacks a detailed examination of the extent to which good hydro simulations support the BGSBU picture. The nearest the literature comes to filling this need is the paper of Jenkins & Binney

⋆ E-mail: mattia.sormani@physics.ox.ac.uk

© 2015 The Authors
Published by Oxford University Press on behalf of the Royal Astronomical Society

Downloaded from https://academic.oup.com/mnras/article/449/3/2421/1121938 by CNRS - ISTO user on 26 April 2022

(1994), which describes simulations that are of low resolution by today's standard, and uses sticky particles rather than a conventional hydro simulation based on the Euler equations. Papers comparing closed orbits with the results of hydro simulations in bar potentials can be found (van Albada & Sanders 1982; Athanassoula 1992a,b), but, for lack of resolution or other reasons, none of them provides sufficient detail to show which orbits are or are not occupied by gas, especially in the vicinity of the cusped orbit, which plays a crucial role in the BGSBU picture.

In this work, we use high-resolution hydrodynamical simulations to re-examine the BGSBU picture. In the first part, we test the extent to which the physics of the gas flow hypothesized by BGSBU is supported by the simulations. Is the gas flow far from the shocks well approximated by closed orbits? Can the gas flow be understood as a transfer from $x_1$ to $x_2$ orbits? Does the transition happen at the cusped orbit as conjectured by BGSBU? We show that the answers these questions depend on the spatial resolution and sound speed used in a hydro simulation. The results are likely to be valid for all barred potentials that have a general resemblance to the BGSBU potential. In the second part of the paper, we discuss the implications of our results for the interpretation of the observational data. Can we identify in the simulations structures reminiscent of the CO parallelogram of BGSBU? Under what conditions does the size of the $x_2$ disc match the region covered by CS emission? Can we explain the high-velocity peaks in the H I $(l, v)$ diagrams at $|v| \simeq 270\,\mathrm{km\,s^{-1}}$ and $|l| \simeq 2^\circ$?

This paper is structured as follows. In Section 2, we present the numerical schemes employed in the simulations. In Section 3, we show the results of the hydro simulations. We discuss the physical interpretation of the simulations in Section 4, and in Section 5 we discuss their implications for the interpretation of observational data. We finally summarize our findings in Section 6.

## 2 METHODS

### 2.1 Hydro simulation scheme

We assume that the gas is a fluid governed by the Euler equations complemented by the equation of state of an isothermal ideal gas. Then we run two-dimensional hydrodynamical simulations in an externally imposed, rigidly rotating barred potential. The output of each simulation consists in snapshots of the velocity and surface density distributions $\rho(\boldsymbol{x})$ and $\boldsymbol{v}(\boldsymbol{x})$ at chosen times.

We use a grid-based, Eulerian code based on the second-order flux-splitting scheme developed by van Albada, van Leer & Roberts (1982) and later used by Athanassoula (1992b), Weiner & Sellwood (1999) and others to study gas dynamics in bar potentials. We used the same implementation of the code as was used by Sormani & Magorrian (2015), slightly modified to implement the recycling law of Athanassoula (1992b).

This recycling law introduces a term in the continuity equation to take into account in a simple way the effects of star formation and stellar mass-loss. The equation governing this process is

$$\frac{\partial \rho}{\partial t} = \alpha(\rho_0^2 - \rho^2), \tag{1}$$

where $\alpha = 0.3\,\mathrm{M_\odot\,pc^{-2}\,Gyr^{-1}}$ is a constant and $\rho_0$ is the initial surface density, which is taken to be $\rho_0 = 1\,\mathrm{M_\odot\,pc^{-2}}$. In practice, the only effect of the recycling law is to prevent too much gas accumulating in the very centre, and it does not affect the morphology of the results. Hence, the results of this paper do not change if we disable the recycling law.

We used a grid $N \times N$ to simulate a square 10 kpc on a side. $N$ depends on the resolution of the simulation. For example, if the grid cells are $\mathrm{d}x = 5\,\mathrm{pc}$ on a side, we have $N = 2000$. In each run, the initial conditions are as follows. We start with gas in equilibrium on circular orbits in an axisymmetrized bar and, to avoid transients, turn on the non-axisymmetric part of the potential gradually during the first 150 Myr, in such a way that the total mass of the underlying potential is conserved in the process. We use outflow boundary conditions: gas can freely escape the simulated region, after which it is lost forever. The potential well is sufficiently deep, however, that very little gas escapes the regions of interest.

### 2.2 The potential

We use the same potential as Jenkins & Binney (1994). This arises from two components. The first is the bar used by BGSBU, which has the density distribution

$$\rho_\mathrm{b}(a) = \rho_{\mathrm{b}0} \begin{cases} (a/a_0)^{-\alpha} & \text{if} \quad a \le a_0 \\ (a/a_0)^{-\beta} & \text{if} \quad a > a_0, \end{cases} \tag{2}$$

where $a = \sqrt{x^2 + (y^2 + z^2)/q^2}$ and the values of the parameters are $a_0 = 1.2\,\mathrm{kpc}$, $\alpha = 1.75$, $\beta = 3.5$, $\rho_{\mathrm{b}0} = 0.69\,\mathrm{M_\odot\,pc^{-3}}$, $q = 0.75$, so the major axis of the bar always lies along the $x$-axis. The second component is a razor-thin exponential disc, which has been added to complete realistically the circular velocity curve outside $R \simeq 1\,\mathrm{kpc}$, and it has little influence inside this radius. The exponential disc is generated by a surface density distribution

$$\Sigma(R) = \Sigma_0 \mathrm{e}^{-R/R_\mathrm{d}}, \tag{3}$$

where $R$ is the radius in cylindrical coordinates and the parameters have values $\Sigma_0 = 1300\,\mathrm{M_\odot\,pc^{-2}}$, $R_\mathrm{d} = 4.5\,\mathrm{kpc}$.

The potential is assumed to be rigidly rotating with constant pattern speed $\Omega_\mathrm{p} = 63\,\mathrm{km\,s^{-1}\,kpc^{-1}}$. This places the Inner Lindblad Resonance at $R_\mathrm{ILR} = 0.6\,\mathrm{kpc}$ and corotation at $R_\mathrm{CR} = 3.7\,\mathrm{kpc}$.

### 2.3 Projecting to the $(l, v)$ plane

We adopt a very simple projection procedure to produce the predicted $(l, v)$ distributions for each simulation snapshot $(\rho(\boldsymbol{x}), \boldsymbol{v}(\boldsymbol{x}))$. Throughout this paper, we assume that the Sun is undergoing circular motion at a radius $R_0 = 8\,\mathrm{kpc}$ with speed $v_\odot = 220\,\mathrm{km\,s^{-1}}$. Calling $\phi$ the angle between the major axis and the Sun–GC line, the Cartesian coordinates of the Sun are given by $x_\odot = R_0 \cos\phi$, $y_\odot = R_0 \sin\phi$. All the projections made in this paper assume $\phi = 20^\circ$.

The resolution of our $(l, v)$ diagrams is $\Delta l = 0.^\circ 25$ in longitude and $\Delta v = 2.5\,\mathrm{km\,s^{-1}}$ in velocity. Along each line of sight, we sample the density and the velocity by linearly interpolating the results of the simulations at points separated by $\delta s = 1\,\mathrm{pc}$. These density measures are accumulated in velocity bins of width $\Delta v = 2.5\,\mathrm{km\,s^{-1}}$. The final $(l, v)$ intensity at the chosen longitude in each range of velocity is the mass in the relevant bin divided by the square of its distance.

This procedure yields a predicted brightness temperature that is linear in column density so it is equivalent to the simplest radiative transfer calculation. In the case of H I, the brightness temperature is linear in the column density if the gas has constant spin temperature and its optical depth is negligible. So our projection is equivalent to simple H I radiative transfer in the constant-temperature, optically thin case. The assumption of constant temperature is known to be a simplification for Galactic H I, which is instead often modelled as a medium made by two or more phases at different temperatures



Downloaded from https://academic.oup.com/mnras/article/449/3/2421/1121938 by CNRS - ISTO user on 26 April 2022

(see for example Ferrière 2001). In the case of $^{12}$CO, the brightness temperature is not linearly related to density when considering a single cloud, but a linear relationship will hold between brightness temperature and the number density of unresolved CO clouds provided the cloud density is low enough for shadowing of clouds to be unimportant (see e.g. Binney & Merrifield 1998, Section 8.1.4).

## 3 RESULTS

Fig. 1 shows a selection of closed orbits in the BGSBU potential, in the frame corotating with the bar. Orbits that BGSBU believed to carry gas are shown by full lines, while those they thought empty are shown by dashed lines. In the outer region, we show a nested sequence of non-self-intersecting $x_1$ orbits that terminates in the cusped orbit, drawn in black. Inside this orbit we show dotted two self-intersecting $x_1$ orbits. The vertically elongated orbits belong to the $x_2$ family, which extends quite a bit beyond the point where the cusped $x_1$ orbit intercepts the vertical axis. BGSBU argued that gas transfers between the $x_1$ and $x_2$ families at the cusped orbit. A primary goal of this paper is to test this conjecture.

Fig. 2 summarizes the results of our simulations. It shows the density of hydro simulations for different grid spacings d$x$ and sound speeds $c_s$. All snapshots are taken at the same time $t = 280$ Myr. Some common features of the gas flow can be identified in all panels. In the outer part, approximately corresponding to the green region, the gas follows $x_1$ orbits. At some point near the $x$-axis, two thin offset shocks emerge, which connect the green region to the reddish central disc. The central disc is called the $x_2$ disc and is made by gas on $x_2$ orbits. Most of the gas plunges to the $x_2$ disc or 'central molecular zone' through the shocks.

Thus, the gas follows the $x_1$ orbits in the outer part and the $x_2$ orbits in the central part, with a transition zone containing the shocks in between. In each simulation, we can identify an innermost occupied $x_1$ orbit. The shocks are formed just after this orbit and they induce the transition from the $x_1$ to the $x_2$ family. We call this innermost occupied $x_1$ orbit the transition orbit, and the transition point its position in a parametrization of the sequence of $x_1$ orbits.

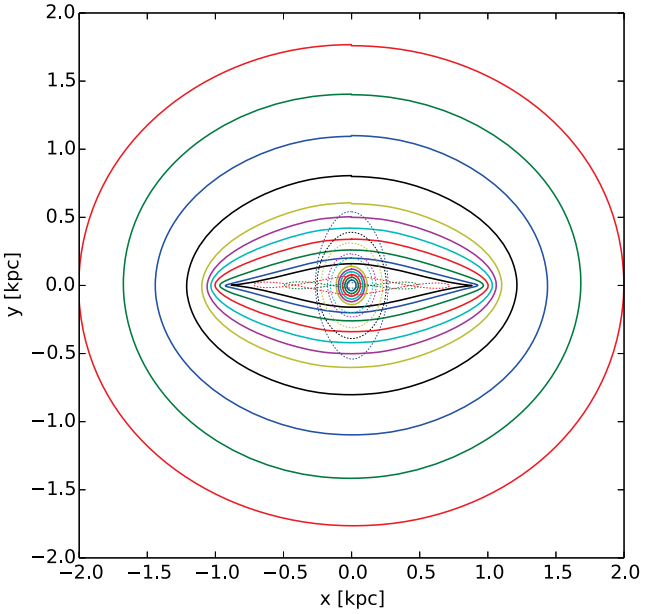



**Figure 1.** $x_1$ and $x_2$ orbits in the potential used by BGSBU. Orbits are shown in the frame that rotates (clockwise) with the bar. The horizontally elongated orbits form the $x_1$ family, while the vertically elongated ones are from the $x_2$ family. BGSBU hypothesized that the orbits drawn in full lines have gas, while orbits those shown dashed are unoccupied. The cusped $x_1$ orbit is the smallest horizontally elongated orbit drawn in full lines and is shown black.

BGSBU assumed that the transition orbit is the cusped orbit. In our simulations, the transition point and the size of the $x_2$ disc depend strongly on both the resolution and the sound speed. Consider, for example, the middle column in Fig. 2, corresponding to $c_s = 10\,\mathrm{km\,s^{-1}}$. As we increase the resolution, the transition point moves inwards while the $x_2$ disc shrinks. At the highest resolution, d$x = 5$ pc, the transition orbit almost coincides with the cusped orbit, as predicted by BGSBU. At lower resolution, the transition happens earlier and the transition orbit is much bigger than the cusped orbit. Fig. 3 shows the same density snapshots as Fig. 2, superimposed on the closed orbits that BGSBU thought carried gas for a better comparison.

Increasing the sound speed also has the effect of postponing the transition and shrinking the $x_2$ disc. Consider, for example, the second row in Fig. 2, corresponding to d$x = 20$ pc. At this resolution, the transition happens very early, for $c_s = 5\,\mathrm{km\,s^{-1}}$, and the transition orbit is quite an outer $x_1$ orbit (approximately the yellow orbit in Fig. 1). As we increase the sound speed, the transition orbit moves inwards, and for $c_s = 20\,\mathrm{km\,s^{-1}}$ it coincides in Fig. 1 with the green orbit that lies just outside the cusped orbit. We will discuss the origins of these systematics in Section 4.

The two highest resolution simulations in the right-hand column of Fig. 2 look peculiar. These correspond to $c_s = 20\,\mathrm{km\,s^{-1}}$ and d$x = 5, 10$ pc. At the time shown, all other simulations have already reached an approximate steady state, and they would not appear significantly different after another 250 Myr or more. These two simulations instead manifest a complex unsteady flow interior to the transition orbit. The shocks are not stable, but keep forming and dissolving in an endless cycle. In some snapshots, they are almost completely formed and smooth (see also Section 4.3 and Fig. 9). At these moments, they lie very close to the $x$-axis. A little later, vortices grow on the leading side, which move around and eventually bump on the opposite shock, creating more vorticity. Later the cycle repeats. Tests described in Section 4.3 suggest that the unsteadiness is real and not an artefact of our particular code.

So far we have not discussed the velocity structure of our simulations, but this is crucial for the interpretation of observations. Fig. 4 shows the projections into the $(l, v)$ plane of the snapshots of Fig. 2 for an assumed angle $\phi = 20^\circ$ between the bar's major axis and the Sun-Galactic Centre line. The lines in Fig. 4 show the $(l, v)$ traces of some of the closed orbits plotted in Fig. 3 using the same colour scheme – we plot only the orbits that BGSBU thought occupied (those shown with full lines in Fig. 1).

For all resolutions and sound speeds, in Fig. 4 the envelope of the outermost $x_1$ orbits matches the envelope of the hydro distribution very well. As we move towards smaller values of $|l|$, the traces of orbits sweep up towards the high-velocity peak of the cusped orbit, but at the transition orbit the hydro envelope starts to fall, and thus becomes separated from the orbit envelope. The projection of the hydro $x_2$ disc is clearly identifiable as a darker region near the centre. At the smallest longitudes, its boundary is delineated by the traces of the $x_2$ orbits, but for low sound speeds or resolutions it extends far beyond the region covered by the plotted $x_2$ orbits.

This finding again confirms the picture of the gas flow that we delineated above. When the transition point is too early, the innermost non-self-intersecting $x_1$ orbits, which are populated by gas in the BGSBU picture, are void of gas in the hydro simulations. Outer $x_2$ orbits that lack gas in the BGSBU picture are occupied

Downloaded from https://academic.oup.com/mnras/article/449/3/2421/1121938 by CNRS - ISTO user on 26 April 2022

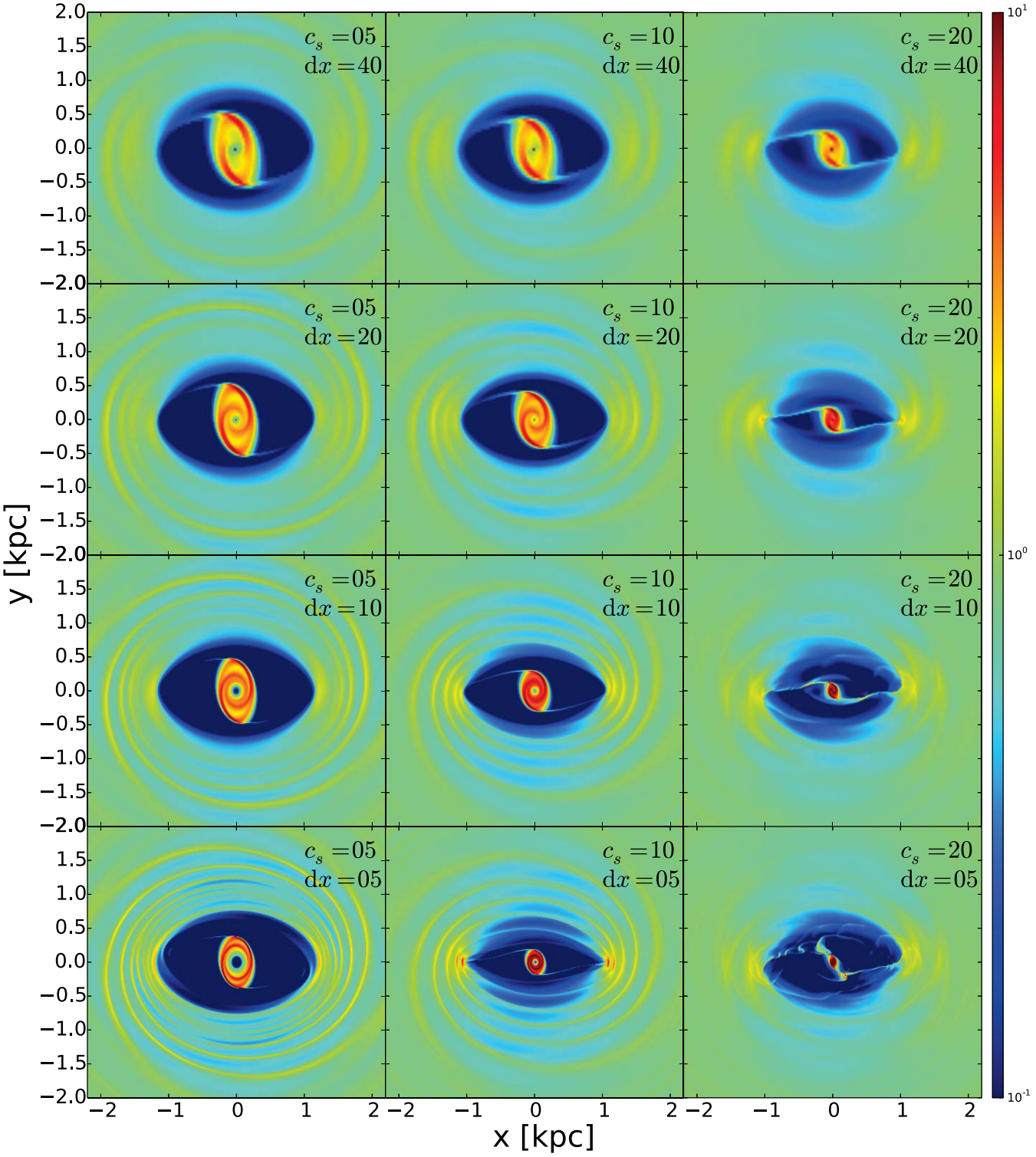



**Figure 2.** The fluid density in hydro simulations in the BGSBU potential for different spatial resolutions and sound speeds. $c_s$ is increasing left to right taking values 5,10,20 km s$^{-1}$. d$x$ is decreasing from top to bottom taking values 40,20,10,5 pc. Gas has reached an approximately steady state in the rotating frame and circulates clockwise. All snapshots are taken at $t = 280$ Myr.

by gas in the hydro simulation. As we increase the resolution at $c_s = 10\,\mathrm{km\,s^{-1}}$ (middle column), the transition between the $x_1$ and $x_2$ families moves inwards, and the hydro envelope matches more and more closely the predictions of the BGSBU picture. At the same time, the projection of the $x_2$ disc shrinks, also approaching the BGSBU picture. Eventually, for d$x = 5$ pc and $c_s = 10\,\mathrm{km\,s^{-1}}$, the envelope of the hydro the projection of the $x_2$ disc match very well as in the BGSBU picture.

At low sound speed (left-hand column of Fig. 4), the transition always happens early, so orbits close to the cusped orbit are



Downloaded from https://academic.oup.com/mnras/article/449/3/2421/1121938 by CNRS - ISTO user on 26 April 2022

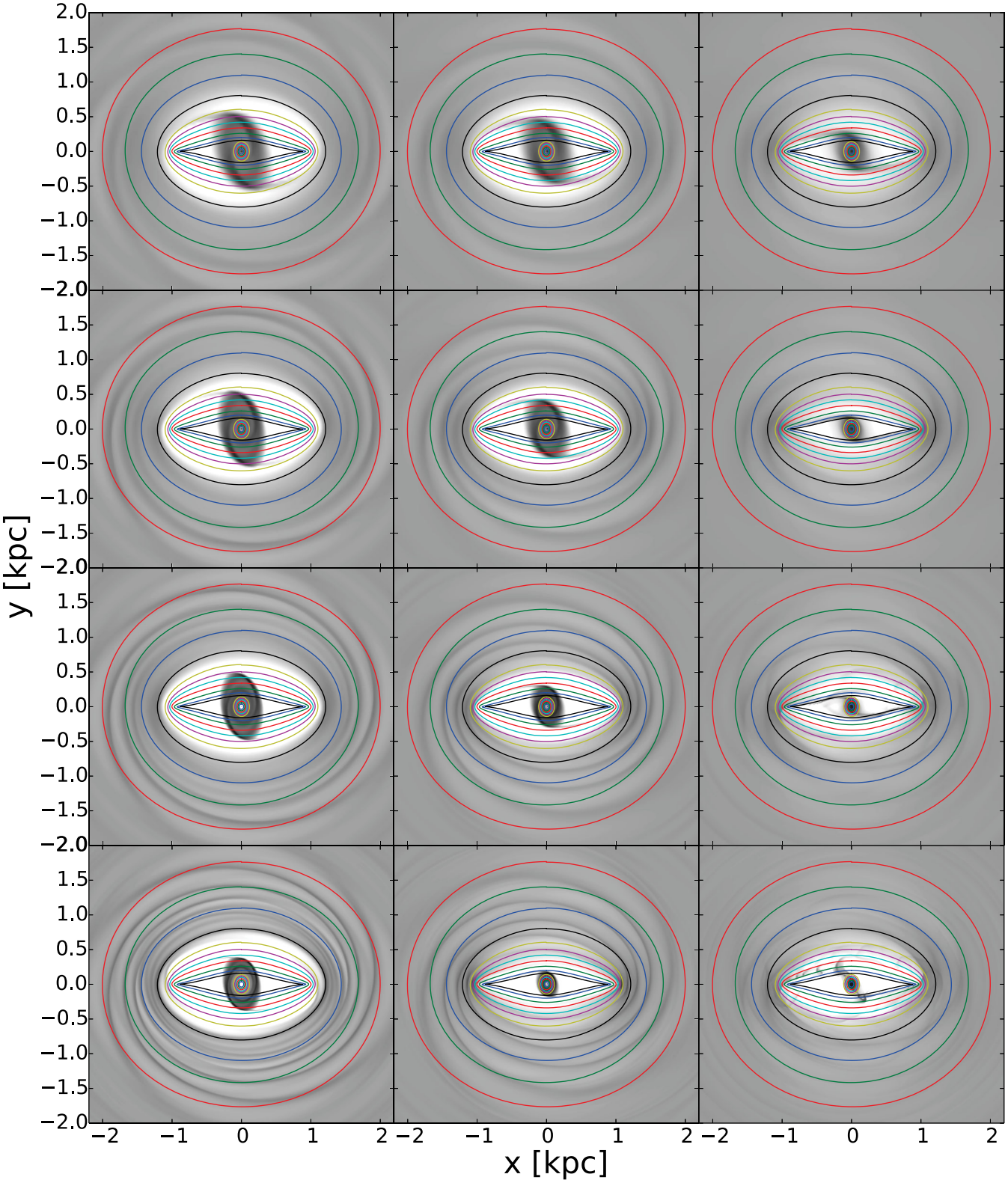



**Figure 3.** Same as Fig. 2 but with superimposed orbits.

unoccupied at all resolutions. Therefore at low sound speeds, the hydro simulations gives results inconsistent with the BGSBU picture. At high sound speeds, the hydro simulations approach the BGSBU picture as we increase the resolution at first. But at higher resolution, unsteadiness makes the projected hydro deviate significantly from the BGSBU picture.

To explain this situation from a face-on perspective, we take as an illustrative example the case $\mathrm{d}x = 10$, $c_\mathrm{s} = 10\,\mathrm{km\,s^{-1}}$. Fig. 5

Downloaded from https://academic.oup.com/mnras/article/449/3/2421/1121938 by CNRS - ISTO user on 26 April 2022

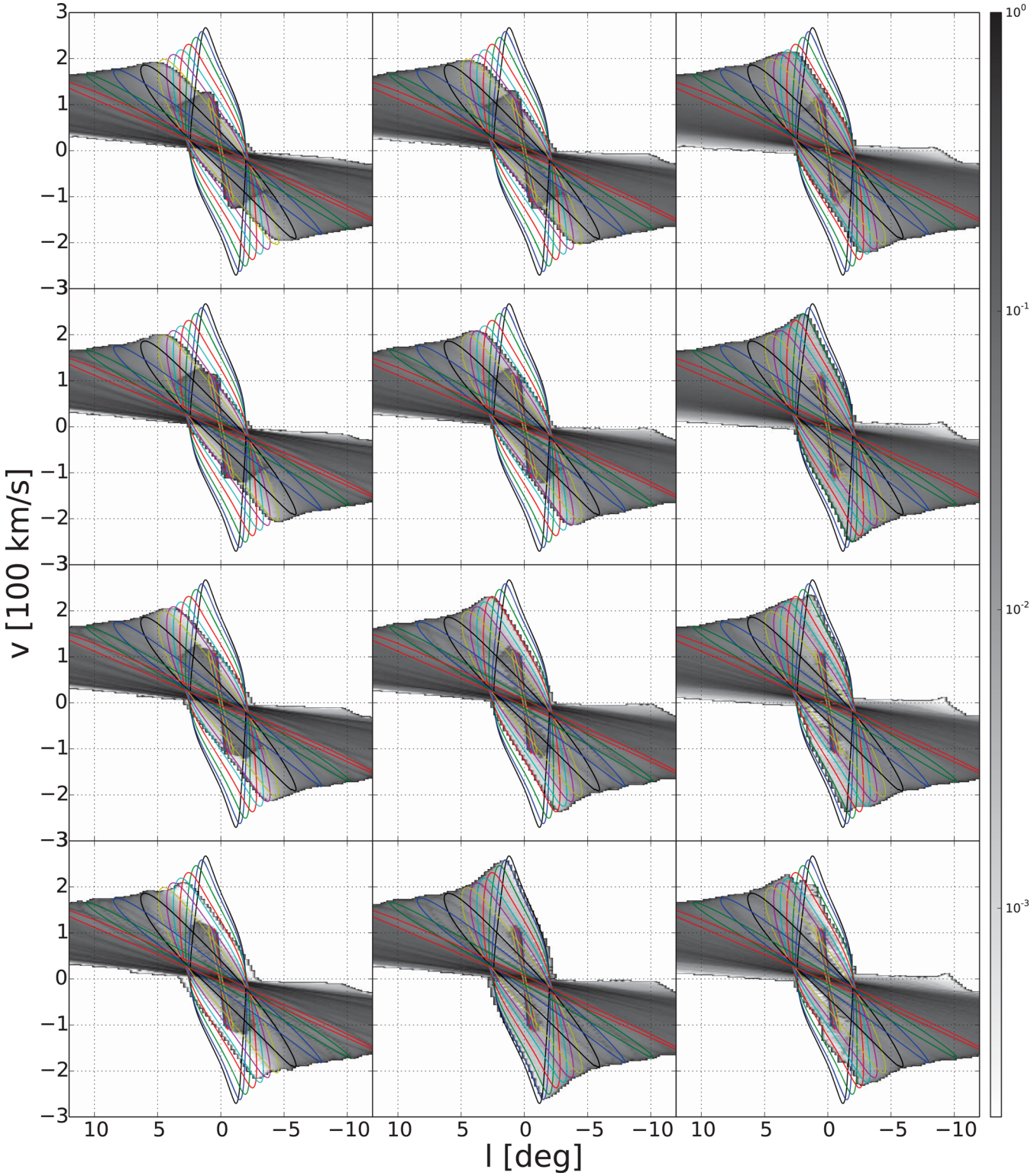



**Figure 4.** The simulations of Figs 2 and 3 projected into the $(l, v)$ plane. Solid lines show the $(l, v)$ traces of closed orbits, with colours matching other figures. The Sun is assumed to be in a circular orbit with $v = 220\,\mathrm{km\,s^{-1}}$ at $R_0 = 8\,\mathrm{kpc}$, and the bar major axis makes an angle $\phi = 20^\circ$ with the Sun-Galactic Centre line.

compares the velocity field of the hydro simulation with that of the closed orbits. The left-hand panel shows the velocity field of the hydro simulation. The central panel shows the best approximation to the hydro velocity field that can be obtained from the $x_1$ and $x_2$ orbits; at each point where more than an orbit is present, we show the velocity of the orbit that best matches the hydro velocity field. In all panels, the density of the hydro simulation is shown in the background. Locations through which no closed orbit passes



Downloaded from https://academic.oup.com/mnras/article/449/3/2421/1121938 by CNRS - ISTO user on 26 April 2022

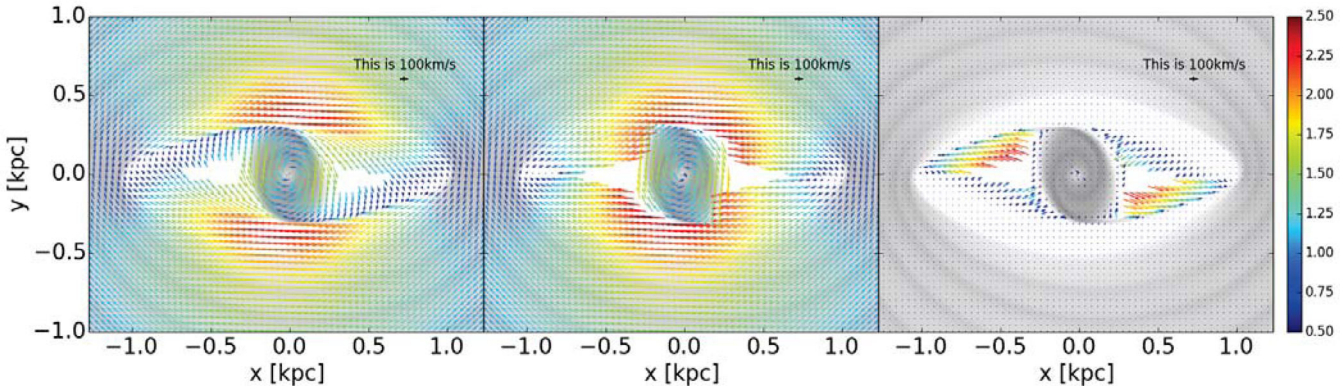



**Figure 5.** Using closed orbits to approximate the hydro velocity field for the simulation with $\mathrm{d}x = 10\,\mathrm{pc}$, $c_\mathrm{s} = 10\,\mathrm{km\,s^{-1}}$ shown at left. The central panel shows the best approximation to that velocity field obtained using closed orbits belonging to $x_1$ or $x_2$ family. For each point where more than one orbit is found, the chosen velocity is the one closest to the hydro velocity. The right-hand panel shows the vector differences between the left-hand and middle panels. In all panels, points without orbits are masked and the density of the hydro simulation is visible in the background. The colourbars show the speed at each point in units of $100\,\mathrm{km\,s^{-1}}$.

are masked out. The right-hand panel is the most interesting panel; it shows the vector difference between the left-hand and middle panels, and shows clearly that the outer $x_1$ orbits and the inner $x_2$ orbits both reproduce the hydro velocity field accurately. The red orbit in Fig. 1 is the transition orbit in this case, the last orbit at which the velocity fields coincide, and is just outside the shocks. After this, the shocks emerge and the two velocity fields suddenly diverge.

At different resolutions and sound speeds, the situation is qualitatively very similar but the point of transition between orbit families changes. For $c_\mathrm{s} = 20\,\mathrm{km\,s^{-1}}$ and high resolution, the hydro flow in the transition region is unsteady.

## 4 THE PHYSICS OF THE GAS FLOW

### 4.1 Dependence on the sound speed

In Section 3, we have seen that as the sound speed increases, the transition point and the shocks move inwards. At the same time, the shocks also become more horizontal and closer to the $x$-axis. Englmaier & Gerhard (1997) and Patsis & Athanassoula (2000) found similar results when varying the sound speed. A qualitative explanation for this behaviour is as follows (for another discussion see also Englmaier & Gerhard 1997).

The more elongated an $x_1$ orbit is, the larger the variation along the orbit in the speed of an orbiting particle. Since the speed decreases as particles move from the orbit's minor axis to its major axis, the density of gas that is streaming along the orbit increases as the major axis is approached. When the sound speed is high, pressure assists gravity in slowing gas as it approaches the major axis, and equally assists gravity in accelerating the flow after the major axis has been passed. In the absence of a shock, the gas is reversibly compressed and decompressed so it can continue to keep close to one orbit for several revolutions.

If the sound speed is too low, the convergence of the gas as the major axis is approached leads to shock formation. Entropy is created in the shock, so the decompression after the major axis has been passed does not reverse what happened as the axis was approached, and the flow deviates strongly from orbits.

The key to avoiding shock formation is the ability of sound waves to carry information about fluctuations in density upstream so oncoming gas can be slowed in a timely manner when the density increases at a downstream location. The nearer the cusped orbit is approached, the larger is the velocity gradient up which sound waves have to travel if a shock is to be avoided. Hence, decreasing the sound speed causes the shock to form further out.

### 4.2 Dependence on numerical resolution

Increasing the resolution moves the orbit at which shocks form inwards with important consequences for the interpretation of the gas flow in our Galaxy that will be discussed in Section 5. A likely explanation for this phenomenon is that at low resolution the innermost $x_1$ orbits are inadequately resolved. To resolve the cusp we need in principle infinite resolution. By increasing the resolution, we can resolve orbits closer and closer to the cusped one, and gas can settle on these orbits, delaying the formation of shocks.

Fig. 6 tests this idea by showing the $(l, v)$ traces of nine orbits from the cusped orbit (at the top) outwards. Each orbit is mapped four times at resolutions that increase from left to right. The faint solid lines show the traces of the orbits and as such are the same along every row. The big points scattered around this line show the $(l, v)$ trace one obtains by associating each hydro cell through which the orbit passes with the mean velocity of its passage, and then projecting the resulting velocities of the visited cell. The small points show the projection at the visited cells of the hydro velocity field for $c_\mathrm{s} = 10\,\mathrm{km\,s^{-1}}$.

We see that orbits that are well outside the cusped orbit (lower part of the figure) are well represented by even the coarsest grid (left-hand side of the figure), and, moreover, their velocities are accurately reproduced by the hydro code. As we move up the figure and therefore approach the cusped orbit, at low resolutions the big dots scatter widely around the orbit's curve. The scatter is widest at the largest values of $|l|$ because that is where the velocity gradient is largest and thus the finite resolution of the grid has its biggest impact. For each orbit outside the cusped orbit there is a resolution finer than which the hydro velocity field is almost the same as the orbital velocity because along that orbit the flow does not encounter a shock.

### 4.3 Unsteady flow

As mentioned in Section 3, the flow becomes unsteady at high sound speed and high resolution. To test whether this phenomenon was an

Downloaded from https://academic.oup.com/mnras/article/449/3/2421/1121938 by CNRS - ISTO user on 26 April 2022

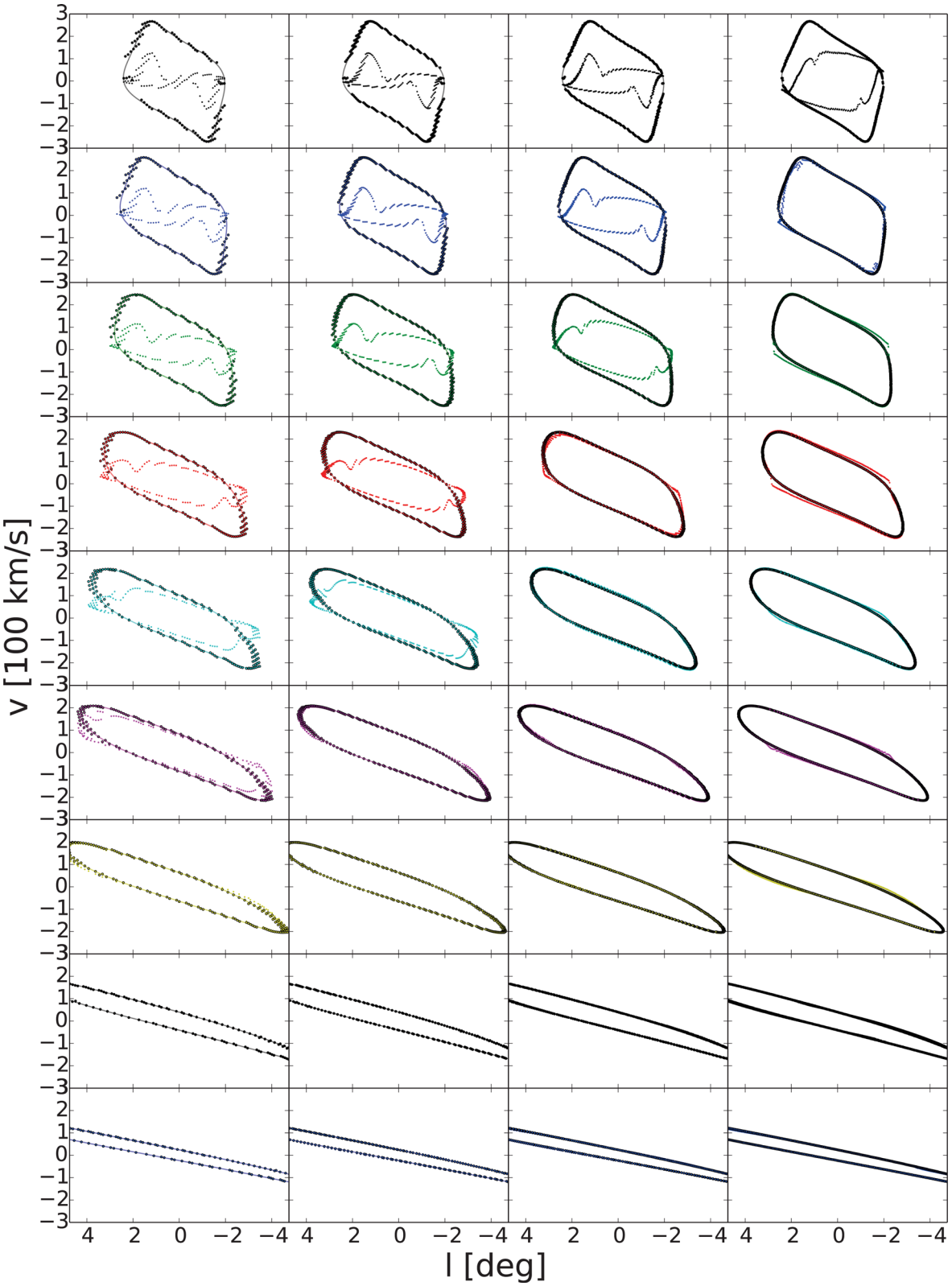



**Figure 6.** Each panel refers to a particular $x_1$ orbit. In full lines, the trace of the orbit. The bigger, empty dots are the velocity field of closed $x_1$ orbits sampled with the same resolution of a hydro simulation along the $xy$ trajectory of the orbit. Smaller, filled dots are the projection of a hydro simulation cells along the same trajectory. Each column refers to one hydro simulations. From left to right, the resolution increases from $\mathrm{d}x = 40\,\mathrm{pc}$ to $\mathrm{d}x = 5\,\mathrm{pc}$. All simulations are for $c_\mathrm{s} = 10\,\mathrm{km\,s^{-1}}$.

Downloaded from https://academic.oup.com/mnras/article/449/3/2421/1121938 by CNRS - ISTO user on 26 April 2022

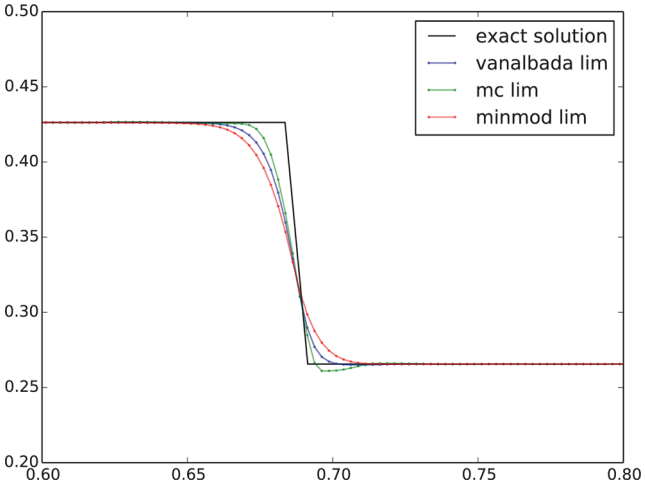



**Figure 7.** Results of SOD shock tube test problem at $t = 0.2$ for different flux limiters. This figure zooms around a shock. The resolution is $dx = 0.0025$.

artefact generated by our code, we re-ran some simulations with a completely different code, PLUTO (Mignone et al. 2007). This is free software for the numerical solution of systems of conservation laws targeting high Mach number flows in astrophysical fluid dynamics. It has a modular structure that makes it easy to change the algorithm used to simulate a flow. We use this modularity to investigate the effects of the choice of Riemann solver and flux limiter. In all of our runs, we used a static Cartesian mesh and RK2 time-stepping. The code was modified to implement our recycling law (1).

We found that the Roe and HLL Riemann solvers produced the same results as each other, and our own code. The choice of flux limiter, by contrast, does have a significant impact on the computed flow; unsteadiness of the flow can be suppressed by changing to a more diffusive flux limiter. Flux limiters are used in numerical schemes to handle the flow close to discontinuities such as shocks. We tested three different limiters and found that unsteadiness is suppressed by choosing a more diffusive limiter, which has a higher numerical viscosity and produces thicker shocks. Fig. 7 shows the result of using PLUTO to perform a standard one-dimensional test problem, the SOD shock tube (Sod 1978). It shows that the three limiters produce shocks of different thicknesses. The most diffusive (more viscosity) is the MINMOD limiter (Roe 1986). The Van Albada limiter used in this paper (van Albada et al. 1982) has intermediate diffusivity, while the least diffusive limiter (least viscosity) is the MC limiter (van Leer 1977). Fig. 8 shows a snapshot at an intermediate time for simulations with $dx = 5\,\mathrm{pc}$, $c_s = 20\,\mathrm{km\,s^{-1}}$ obtained using PLUTO. The only difference between the three simulations is the limiter used. From top to bottom the figure shows the flows obtained with limiters of increasing diffusivity. The top flow has much irregular and unsteady structure that is completely absent from the bottom flow. The central panel shows an intermediate level of unsteady structure.

In these flows unsteady features seem to arise at the shocks, which develop wrinkles that shed vortices. The vortices then move away from the shocks. Vorticity is generated at the shocks and propagates away from them into the body of the flow.

Fig. 9 shows the flow computed with the most diffusive limiter (MINMOD) at three different times. It shows the shocks cyclically straightening out and then developing wrinkles. More unstable simulations also display a cyclical tendency for the shocks to straighten out and dissolve, but in these lower diffusivity calculations the dissolution of the shocks is more sudden. From these tests, we conclude

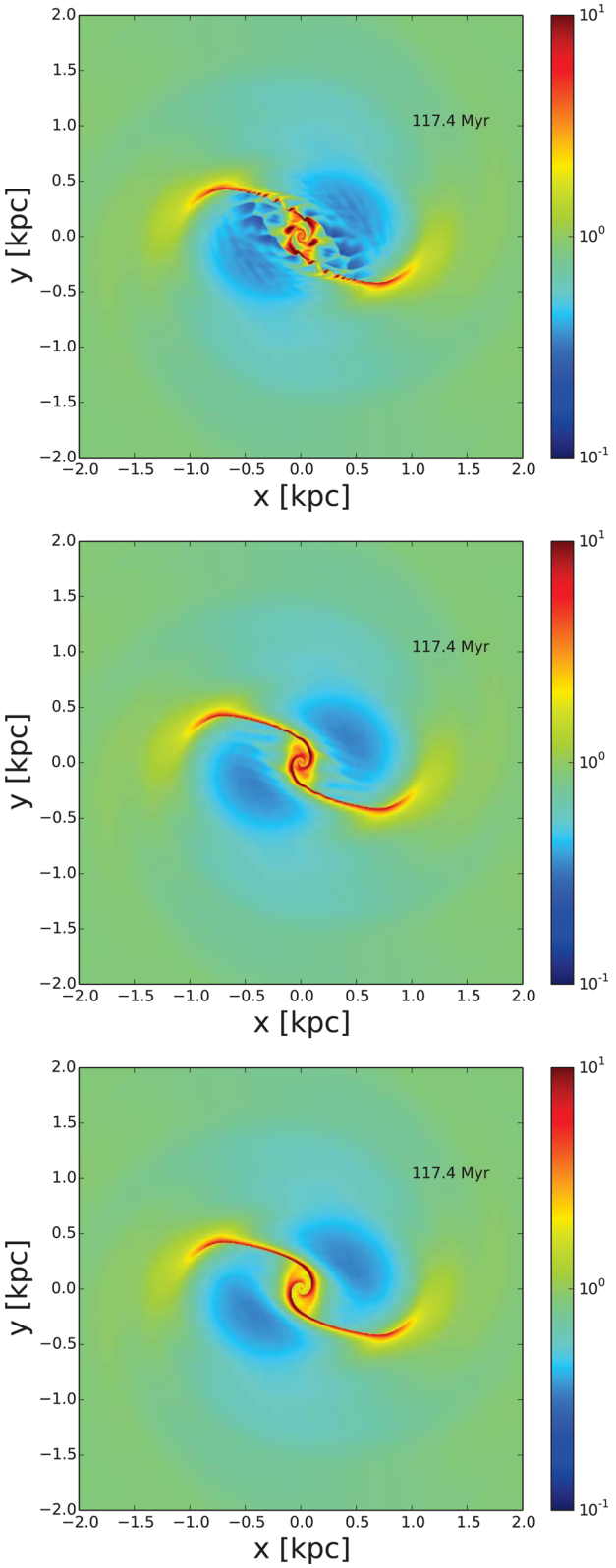



**Figure 8.** Three snapshots capturing the moment when the instability is forming. The three snapshots come from three different simulations obtained with the PLUTO code. The only difference between the three is the limiter used. On top using the MC limiter, middle the VanAlbada limiter and bottom the MidMod limiter.

Downloaded from https://academic.oup.com/mnras/article/449/3/2421/1121938 by CNRS - ISTO user on 26 April 2022

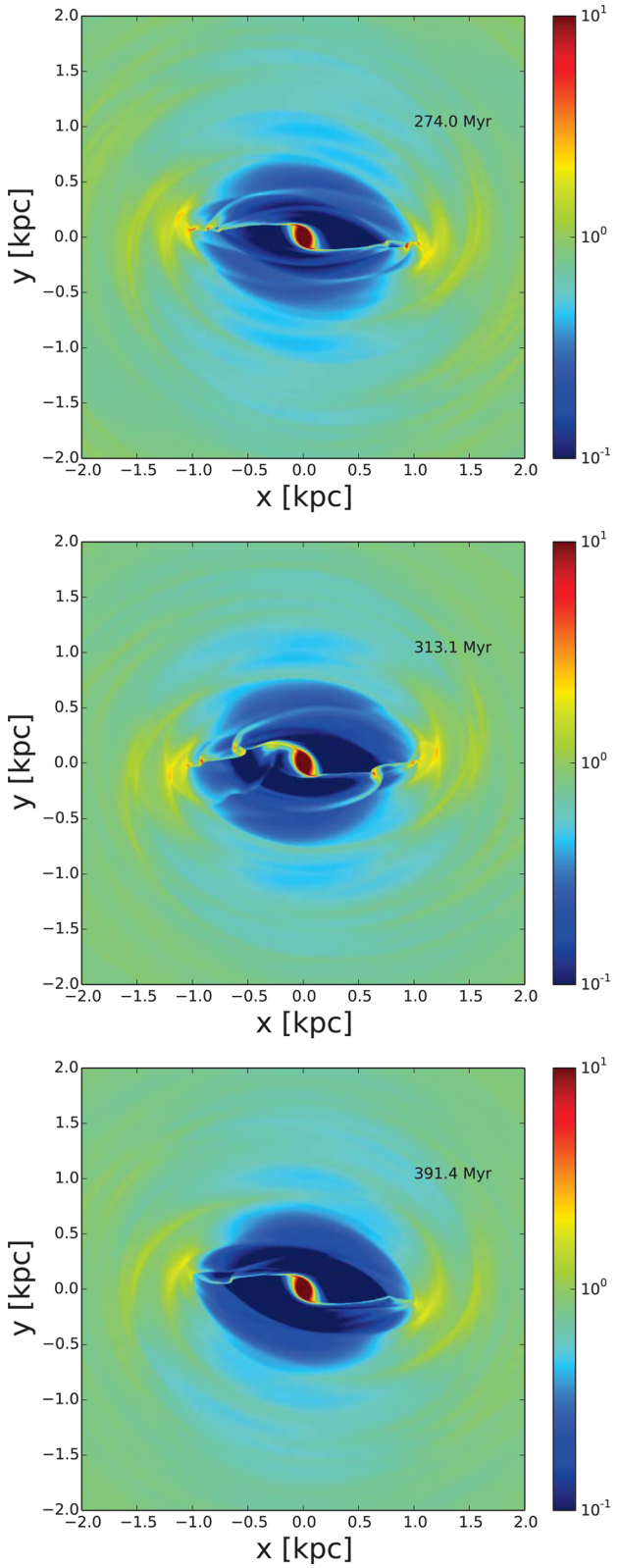



**Figure 9.** Three late snapshots of a simulation using PLUTO code and the MINMOD limiter. This limiter allows the simulation to be only weakly unstable. It shows that shocks are almost formed and destroyed cyclically. Swirls produced at one shock can propagate and bump on the shock on the other side.

that unsteadiness is not a feature of our particular hydro code, but is shared by other well tested codes as well.

Turbulence is a consequence of high rates of shear in a high Reynolds number flow. In the flows studied by engineers, for example in pipes and over aircraft wings, turbulence arises in the thin boundary layer that forms when a low-viscosity fluid meets a solid surface. Vortices formed in the boundary layer move into the bulk of the fluid, making the flow generally unsteady. In our simulations, vortices form along the shocks (see Binney 1974, for an analysis of vorticity generation in shocks), where the shear rate is exceptionally high. The rate of shear is inversely proportional to the width of the shock, so it increases with the grid resolution and decreases with the diffusivity of the limiter. Thus simulations with the finest grids and the least diffusive limiters have the highest shear rates and are most likely to become turbulent.

The fact that turbulence appears only in simulations with a high sound speed can also be explained by the connection between shear rate and the onset of turbulence; the rate of shearing increases along the sequence of $x_1$ orbits as one approaches the cusped orbit, so at low sound speeds, when the shock forms far from the cusped orbit, the maximum rate of shearing is smaller than when the sound speed is larger.

A good indicator of the amount of shear in a 2D flow is the quantity (see for example Maciejewski 2008)

$$\tau^2 = \left(\frac{\partial v_x}{\partial y} + \frac{\partial v_y}{\partial x}\right)^2 + \left(\frac{\partial v_x}{\partial x} - \frac{\partial v_y}{\partial y}\right)^2 . \tag{4}$$

This quantity is invariant under rotations of the coordinates, being the magnitude of the eigenvalues of the traceless shear tensor, defined by

$$D_{ij} = \frac{1}{2}\left(\frac{\partial v_i}{\partial x_j} + \frac{\partial v_j}{\partial x_i} - \delta_{ij}(\nabla \cdot \boldsymbol{v})\right) . \tag{5}$$

Fig. 10 shows the quantity $\tau \mathrm{d}x$, where the shear $\tau$ is estimated by finite differences. As claimed above, the shearing rate is high along the shocks and is higher for higher sound speeds.

Kim et al. (2012a) also encountered the onset of turbulence as isothermal gas moves in a rotating barred potential, and our Fig. 8 is similar to their fig. 4, panel (c). They point out that vortices generated in one shock pass to the shock on the other side of the galaxy, and are there amplified. This process has been called the wiggle instability (see for example Wada & Koda 2004; Kim, Kim & Kim 2014, and references therein). There is still no consensus on the nature of this instability; Wada & Koda (2004) conjectured it is a Kelvin–Helmholtz (KH) type instability, but Kim et al. (2014) use a shearing box analysis to argue it should be considered as a different type of instability. The instability has also been attributed to a numerical noise caused by the discretization of the fluid equations (Hanawa & Kikuchi 2012).

### 4.4 Numerical convergence

We have seen that as we increase the resolution at given sound speed, the shocks are postponed and the $x_2$ disc shrinks. Have we converged, or would a further increase in resolution produce significant changes in the flow? In order to discuss this, let us consider how the size of the $x_2$ disc depends on the resolution. In each snapshot in our simulations, the vertical edges of the $x_2$ disc can be clearly identified by a sharp variation in the gas density as we move along the vertical axis. Consequently, the vertical size of the $x_2$ disc is well defined.



Downloaded from https://academic.oup.com/mnras/article/449/3/2421/1121938 by CNRS - ISTO user on 26 April 2022

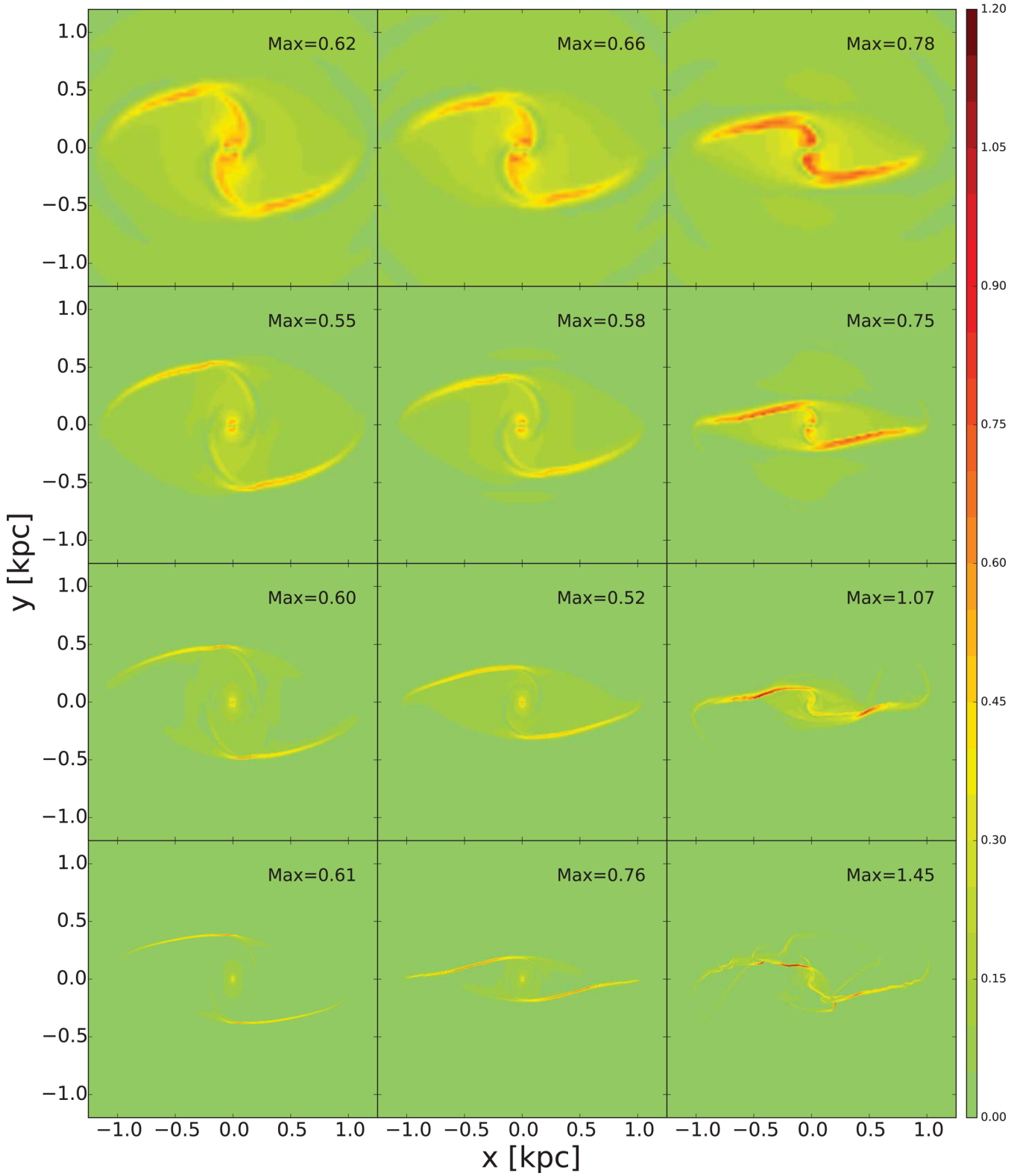



**Figure 10.** The quantity $\tau \mathrm{d}x$, where $\tau$ is an indicator of the shear and is defined in equation (4). In each panel, the maximum value reached by the quantity is shown.

Fig. 11 shows the vertical radius of the $x_2$ disc plotted against resolution for simulations with sound speed $c_s = 10\,\mathrm{km\,s^{-1}}$. The data points for $\mathrm{d}x \geq 5\,\mathrm{pc}$ are from the simulations presented above, while the black dot at $\mathrm{d}x = 2.5\,\mathrm{pc}$ is obtained for an additional simulation. Since the computational cost of a simulation of given spatial extent rises as $(\mathrm{d}x)^{-3}$, the additional simulation was run on a grid that covered an area only 5 kpc × 5 kpc in extent – we have verified that the results of lower resolution simulations for the region

Downloaded from https://academic.oup.com/mnras/article/449/3/2421/1121938 by CNRS - ISTO user on 26 April 2022

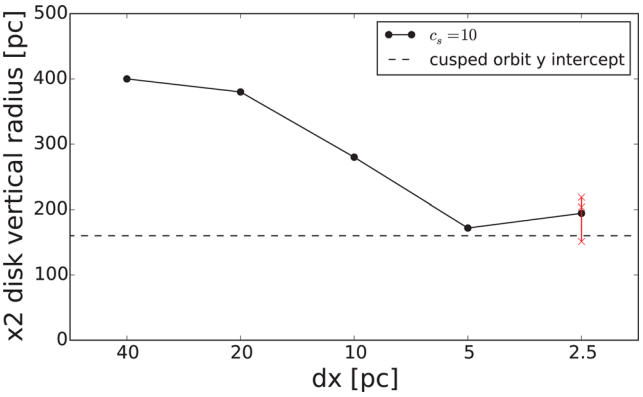



**Figure 11.** The vertical radius of the $x_2$ disc as a function of resolution. Each point is obtained averaging the radius over four different snapshots at times $t = 274, 313, 352, 391$ Myr. For resolution $\mathrm{d}x = 2.5$ pc, the flow is unsteady and the size of the disc fluctuates, and the red crosses show the scatter in the size of the $x_2$ disc over the four snapshots. The horizontal dashed line shows the value of the intercept of the cusped orbit with the vertical axes.

inside the shocks are unaffected by a reduction of the extent of the grid, so the additional simulation should provide a valid additional datum for the radius of the $x_2$ disc.

The simulation with $\mathrm{d}x = 2.5$ pc was unsteady as expected, given the tendency for unsteadiness to arise at high resolutions and sound speeds. On account of the unsteadiness, the size of the $x_2$ disc in the $\mathrm{d}x = 2.5$ pc simulation fluctuates. In Fig. 11, the point for the $\mathrm{d}x = 2.5$ pc simulation is obtained by averaging the $x_2$ disc size over four different snapshots at times $t = 274, 313, 352, 391$ Myr, and the red crosses show the values in each snapshot. Such averaging would not modify the data points for the coarser, steady, simulations. Since in the simulation with $\mathrm{d}x = 2.5$ pc the mean radius of the $x_2$ disc is compatible with this radius when $\mathrm{d}x = 5$ pc, we conclude that the size of the $x_2$ disc has converged to near its true value at $c_\mathrm{s} = 10\,\mathrm{km\,s^{-1}}$.

As can be seen from Fig. 11, the value of the vertical radius towards which we have converged for $c_\mathrm{s} = 10\,\mathrm{km\,s^{-1}}$ is the value of the intercept of the cusped orbit with the vertical axis. Inspection of Fig. 2 shows that for higher sound speeds, the $x_2$ disc becomes smaller. Indeed, Englmaier & Gerhard (1997) found that the $x_2$ disc disappears for high enough sound speed.

### 4.5 A paradox

In the limit of vanishing pressure, the characteristics of the Euler equations reduce to ballistic trajectories. Hence, we expect the ballistic approximation to fluid flow to work best when the sound speed is low. Why is the BGSBU picture, which is founded on the ballistic approximation, more accurately reproduced with $c_\mathrm{s} = 10\,\mathrm{km\,s^{-1}}$ than with $c_\mathrm{s} = 5\,\mathrm{km\,s^{-1}}$?

The answer is that the BGSBU picture includes the requirement that the transition between orbit families lies close to the cusped orbit. This transition is effected by shocks, which are more rather than less likely to form in the limit of vanishing pressure. Shocks reflect the necessity in a fluid for there to be a unique velocity at each spatial point. As Riemann (1860) showed, in certain circumstances the Euler equations predict more than one velocity at a given point of a fluid in the sense that characteristics of the same family can cross. The unphysical implications of crossing characteristics are voided by a shock forming near the crossing point. In the shock, the finite mean-free path of the fluid's constituent particles becomes important, and the Euler equations, which are based in the fiction that the fluid forms a continuum, cease to be valid.

In a region of the disc where there are two distinct families of closed orbits, the principle that in the limit of vanishing pressure the streamlines/characteristics will be closed orbits does not suffice to determine the flow. One needs in addition some way of selecting one orbit family for the streamlines. Since the $x_1$ orbits do not exist at very small radii and the $x_2$ orbits do not exist at very large radii, it is evident that in a barred galaxy the flow must at some point transition from $x_1$ to the $x_2$ orbits. Our simulations have shown that the location of the transition is controlled by the pressure even though the latter is too weak to be dynamically significant upstream of the transition. BGSBU argued that the transition occurs at the cusped orbit, the latest that it could occur, and with hindsight it is not surprising that this requires that the sound speed is $\gtrsim 10\,\mathrm{km\,s^{-1}}$.

### 4.6 Sound speed and the nature of the ISM

Our results can reproduce BGSBU predictions only for a particular sound speed. Does this mean we are providing a measurement of the sound speed?

In addressing this question, a major issue is that we have investigated only one potential and only a single value of the pattern speed, so we cannot exclude the possibility that in another potential the data could be fitted with a lower value of $c_\mathrm{s}$. A trivial illustration of this fact is provided by one of the axisymmetric potentials that were used to interpret $(l, v)$ plots before BGSBU. However, the sharply peaking circular-speed curves that these potentials require to fit the H I envelope in the $(l, v)$ plane are highly implausible, and if the mechanism proposed by BGSBU for generating this feature is to work, gas must stay close to $x_1$ orbits until rather close to the cusped orbit. That is, in a model with a small value of $c_\mathrm{s}$, the upward rise in the H I envelope would have to be at least partly explained by inward-increasing values of the circular speed. Moreover, the cusped orbit would have to occur at smaller radii than BGSBU hypothesized.

Given the almost fractal nature of the interstellar medium (ISM), the physical significance of the parameter $c_\mathrm{s}$ that plays such an important role in the simulations is far from evident. It is, however, worth noting that we have pushed the resolution so high that the cell size of our simulations is comparable to the size of a giant molecular cloud – even small GMCs are $\gtrsim 5$ pc across.

## 5 IMPLICATIONS FOR THE INTERPRETATION OF OBSERVATIONAL DATA

### 5.1 BGSBU revisited

The three key points in BGSBU's interpretation of the observational $(l, v)$ plots were as follows.

(i) The high velocities, reaching $v \simeq 270\,\mathrm{km\,s^{-1}}$, found in the H I $(l, v)$ data could be explained by gas moving on $x_1$ orbits just outside the cusped orbit. When the $(l, v)$ plots had been interpreted in the context of an axisymmetric Galaxy in previous studies (see for example Sofue 2013), the high velocities observed had required the circular-speed curve to first rise, and then fall with implausible rapidity. By hypothesizing a bar, BGSBU were able to explain the sharp peaks in the $(l, v)$ envelope with a monotonically rising circular-speed curve.



Downloaded from https://academic.oup.com/mnras/article/449/3/2421/1121938 by CNRS - ISTO user on 26 April 2022

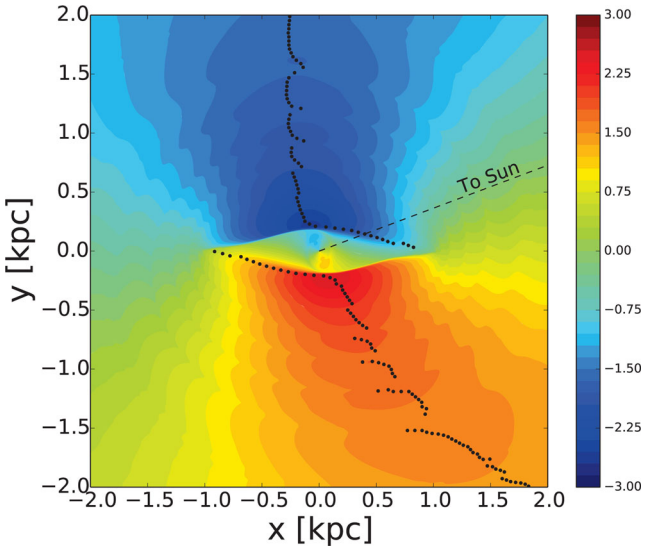



**Figure 12.** The distribution of the projected line-of-sight velocity in the $xy$ plane for the model $\mathrm{d}x = 05\,\mathrm{pc}$, $c_s = 10\,\mathrm{km\,s^{-1}}$. The black dots show the points corresponding to the envelope of gas in the $(l, v)$ plane. The angle between the Sun-Galactic Centre line and the bar major axis is assumed to be $\phi = 20^\circ$. The colourbar is in units of $100\,\mathrm{km\,s^{-1}}$.

(ii) The parallelogram they identified in the CO emission was a cut version of the longitude–velocity trace of the cusped orbit. The discrepancy between the cusped orbit and the CO parallelogram was attributed to the limits of the ballistic approximation, and it was hoped that full hydrodynamical calculation would resolve this discrepancy. In particular, BGSBU pointed to the hydrodynamical simulations of Athanassoula (1992b), which used the same numerical method as this paper, to construct a qualitative argument that qualitatively resolved the discrepancy.

(iii) The emission at low longitudes visible in the CS was attributed to gas on $x_2$ orbits. Outer $x_2$ orbits that can be found in the potential (see Fig. 1) were assumed to be unoccupied by gas.

In the previous section, we confirmed that the flow of gas can be understood as a transfer from $x_1$ to $x_2$ orbits. However, the transition point is not always at the cusped orbit, as BGSBU assumed, but depends on the parameters of the gas flow, especially the sound speed. For the right sound speed, $c_s = 10\,\mathrm{km\,s^{-1}}$, and our maximum resolution, $\mathrm{d}x = 5\,\mathrm{pc}$, the gas flow is very similar to that hypothesized by BGSBU. We now re-analyse the observational data in light of this particular simulation. Further below, we take a step back and discuss interpretation of data in a broader view.

In the centre-bottom panel of Fig. 4, we can see the $(l, v)$ plot corresponding to the simulation with $\mathrm{d}x = 5\,\mathrm{pc}$ and $c_s = 10\,\mathrm{km\,s^{-1}}$. The envelope of the hydro follows that of the closed orbits very well and reproduces the high-velocity peaks found in observations. Fig. 12 shows how the line-of-sight velocity varies in the $xy$ plane for the assumed observing angle $\phi = 20^\circ$. The black dots show the locations that generate the envelope of emission in the $(l, v)$ plane. We can see that the high-velocity peaks at $|l| \simeq 2^\circ$ arise from gas that lies very nearly along an $x_1$ orbit just outside the cusped orbit, as well as the portion of envelope that runs from the peak down into the zone of forbidden velocities. Thus item (i) above is nicely confirmed by this hydro simulation.

Well outside the cusped orbit, the black dots in Fig. 3 have wiggles associated with spiral arms that run out from the extremities of the bar. These wiggles are reflected in small oscillations in the $(l, v)$ envelope, qualitatively similar to what is observed for the envelope of real observations.

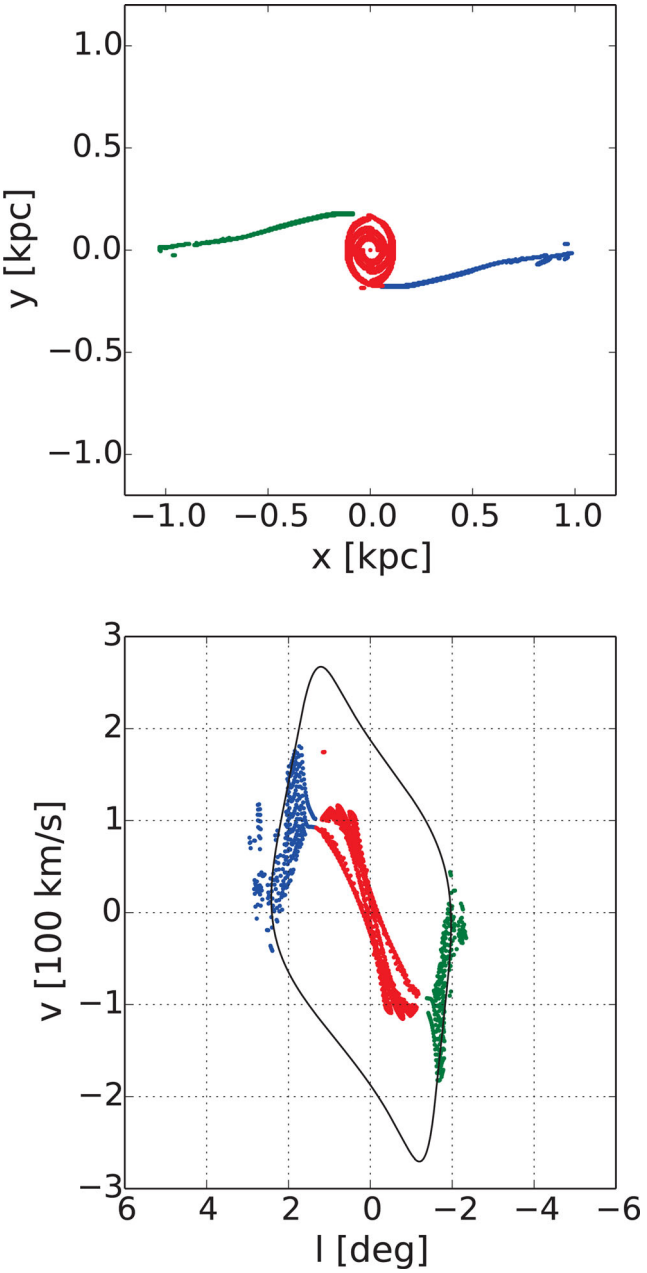



**Figure 13.** Top: points on the narrow shocks and the $x_2$ disc in the $xy$ plane. Bottom: their projected position in the $(l, v)$ plane. In black, the trace of the cusped orbit is shown.

As mentioned above, two distinct structures resembling a parallelogram play a role in the BGSBU picture: one is the CO parallelogram, presumed to be a cut version of the cusped $x_1$ orbit, and second is the trace of an $x_1$ orbit just outside the cusped orbit, which is responsible velocity peaks in the envelope of H I emission. In the simulated $(l, v)$ plots, we can identify only one such parallelogram, namely the second one. How can we solve this inconsistency? Fig. 13 shows the shocks (blue and green) and the $x_2$ disc (red) in the $xy$ plane (top) and in the $(l, v)$ plane (below). In the lower panel, the shocks closely follow the vertical sides of the cusped orbit's (black) parallelogram, but are cut almost exactly where the CO parallelogram ends. We conclude that the vertical sides of the

Downloaded from https://academic.oup.com/mnras/article/449/3/2421/1121938 by CNRS - ISTO user on 26 April 2022

CO parallelogram are formed by shocks. The other two sides of the CO parallelogram must be made up of gas flowing from one shock to the other. The shocks do not show up in our $(l, v)$ projection of the gas flow, though they are quite apparent in the $xy$ plane. In reality, we expect the shocked gas to be brighter than our simple minded radiative calculation suggests, because a lot of atomic gas is converts to molecular as it is compressed at the shocks. When this effect is taken into account the second parallelogram should appear in the $(l, v)$ projection of the model. Thus we confirm item (ii) above of BGSBU's interpretation, although the physical mechanism that causes the parallelogram to be cut was not exactly described by BGSBU. Finally, Fig. 13 clearly shows that in the $(l, v)$ plane the central molecular zone (red) occupies the region of the inner $x_2$ orbits, as conjectured by BGSBU [item (iii) above].

When the $x_1/x_2$ transition happens well before the cusped orbit because either the sound speed or the resolution is low, there is no gas able to explain the high-velocity peaks as in item (i). Moreover, the shocks project to $|l| > 2^\circ$ so they cannot be associated with part of the CO parallelogram, and the central molecular zone is predicted to extend to higher $|l|$ than where significant CS emission is found, compromising the interpretation of item (iii). Thus, several different aspects of the data point to gas remaining on $x_1$ orbits right up to the cusped orbit.

### 5.2 The asymmetry

It is well known that the molecular emission in the central molecular zone is highly asymmetric; three quarters of the $^{13}$CO and CS emission comes from positive longitudes. Perspective effects cannot account for this asymmetry (Jenkins & Binney 1994), so the observed asymmetry must be transient; observations made tens of megayears in the past or future would often show asymmetry in the opposite sense. Thus the likely explanation of the asymmetry is unsteady flow, and the principal motivation of the work reported in Jenkins & Binney (1994) was to find evidence of unsteady flow. Although low-amplitude unsteadiness was generated in their simulations, the present study implies that their simulations were too crude to probe the physically interesting regime.

We saw above that the greater prominence of the CO rectangle in the observed $(l, v)$ plot than in the theoretical $(l, v)$ plot suggests that the shocks are important sites for the conversion of atomic to molecular gas. This being so, unsteady flow through the shocks will give rise to unsteady conversion of atomic to molecular gas, so the atomic/molecular ratio on each side of the centre could well fluctuate as widely as the observations imply. However, a full explanation of the observed asymmetries in molecular-gas emission must await high-resolution simulations that keep track of the chemistry of the ISM.

### 5.3 What do we still need to explain in the $(l, v)$ diagram?

Two aspects of observations remain inadequately explained.

(i) Coherent broad features like the 3 kpc arm and its counterpart on the far side of the Galaxy (Dame & Thaddeus 2008). These are not produced in our simulations. They *are* produced in other hydro simulations (Mulder & Liem 1986; Rodriguez-Fernandez & Combes 2008), but these simulations did not reproduce the high peaks in the envelope of H I emission in the $(l, v)$ plane, probably for lack of resolution.

(ii) Forbidden emission at large longitudes. The portion of the $(l, v)$ diagram covered by forbidden emission in our simulations is smaller than the region in which coherent forbidden emission is seen in the data. A higher quadrupole moment is probably needed to reproduce this.

The essential elements of the BGSBU picture are that streamlines coincide with $x_1$ and $x_2$ orbits, and that the shocks responsible for the transition lie near the cusped orbit. BGSBU illustrated these principles with one particular, very simple potential. Better fits to the data could surely be obtained with other, similar potentials. A fast way to select potentials worthy of closer examination would be to use closed orbits as BGSBU did.

### 5.4 Relation to prior work

The question of what physical mechanism determines the size of the $x_2$ disc is relevant for the interpretation of observations in our and external galaxies (see for example Combes 1996; Kim, Seo & Kim 2012b). Our results suggest that some previous studies may be biased by not taking into account the effects of varying the resolution. For example, Cole et al. (2014) in their simulations of galaxy formation found that the main mismatch between their models and the observations was that the nuclear discs of their models were too big relative to their bars. Since nuclear discs are $x_2$ discs, our results suggest that the mismatch would be resolved by an increase in resolution.

Finally, we mention that our findings do support the hopes of Bissantz et al. (2003). These authors found, as in our low-resolution simulations, that innermost non-self-intersecting $x_1$ orbits near the cusped orbit were unoccupied, and attributed this fact to details of the smoothed particle hydrodynamics scheme, which do not apply for our grid-based simulations. This work gives strong support to their view that in higher resolution, grid-based simulations their inner $x_1$ orbits would be occupied by gas, giving rise to peaks in their $(l, v)$ projections.

## 6 CONCLUSION

(Binney et al. 1991, BGSBU) constructed a picture of the flow of gas through the central few kiloparsecs of our Galaxy. Their picture was based on the idea that gas follows closed orbits, and it involved a particular choice of orbit at which the gas transitions from the $x_1$ orbit family to the $x_2$ family. Their orbit-based picture required validation by hydrodynamical simulations of gas flow. Early efforts in this direction did not provide the necessary validation, in part because they did not adopt the same Galactic potential as BGSBU, but largely because in them gas occupied some $x_2$ orbits that BGSBU required to be empty, and left empty some $x_1$ orbits that BGSBU required to be occupied. We have run high-resolution, grid-based hydro simulations of gas flow in the potential of BGSBU and validated their picture in the case that the effective sound speed in the ISM is $c_s \gtrsim 10\,\mathrm{km\,s^{-1}}$.

The simulations confirm that, regardless of the sound speed adopted and the grid resolution employed, gas streamlines closely coincide with closed orbits everywhere outside a shock-dominated transition region that divides the outer region, in which gas follows $x_1$ orbits, from an inner region, in which gas follows $x_2$ orbits. However, the orbit at which the shock arises, and the transfer commences, depends on both the sound speed and the grid's resolution. Shock formation is favoured by both low sound speeds and low grid resolutions, so increasing the sound speed and/or the grid resolution moves inwards the shock that causes gas to plunge from $x_1$ to $x_2$ orbits. The BGSBU picture calls for the shock to occur as close to



Downloaded from https://academic.oup.com/mnras/article/449/3/2421/1121938 by CNRS - ISTO user on 26 April 2022

the Galactic Centre as it logically can, namely at the cusped orbit, interior to which $x_1$ orbits become self-intersecting. Consequently, a flow consistent with the BGSBU picture cannot be obtained with either a low sound speed or poor spatial resolution. It seems that previous simulations lacked the requisite resolution. We find that a consistent flow can be obtained for $c_s \simeq 10\,\mathrm{km\,s^{-1}}$ and grid spacing $\mathrm{d}x \lesssim 5\,\mathrm{pc}$.

BGSBU did not provide a satisfactory explanation of the parallelogram-like structure of CO emission in the $(l, v)$ plane. We find that the shocks form two sides of the CO parallelogram and conjecture that the prominence of the CO parallelogram is due to efficient conversion of atomic gas into molecular gas. Unfortunately, we do not follow the ISM's chemistry.

In our highest resolution simulations, the flow in the transition region between the $x_1$ and $x_2$ orbits is unsteady. We think this unsteadiness is probably a real physical phenomenon rather than a computational artefact, and is essentially turbulence generated in the region of high shear behind the shocks. We consider this unsteadiness, in conjunction with efficient conversion of atomic gas to molecular form in the shocks, provides a promising explanation of the observed asymmetry in the distribution of CO emission either side of the Galactic Centre.

While our simulations do provide strong support for the BGSBU picture, they do not explain all aspects of the observed H I and CO emission. There is, however, every prospect that further high-resolution simulations of flows in potentials similar to that used by BGSBU will explain all significant features. In this connection, two very worthwhile upgrades of our simulations would be an increase in the quadrupole moment of the bar, and inclusion of the conversion of gas between atomic and molecular forms.

## ACKNOWLEDGEMENTS

We are grateful to Witold Maciejewski for helpful comments. MCS acknowledges the support of the Clarendon Scholarship Fund and is indebted to Steven N. Shore and Mir Abbas Jalali for helpful discussions. JB and JM were supported by Science and Technology Facilities Council by grants R22138/GA001 and ST/K00106X/1. JM acknowledges support from the 'Research in Paris' programme of Ville de Paris. The research leading to these results has received funding from the European Research Council under the European Union's Seventh Framework Programme (FP7/2007-2013) / ERC grant agreement no. 321067.

## REFERENCES

Athanassoula E., 1992a, MNRAS, 259, 328
Athanassoula E., 1992b, MNRAS, 259, 345
Baba J., Saitoh T. R., Wada K., 2010, PASJ, 62, 1413
Binney J., 1974, MNRAS, 168, 73
Binney J., Merrifield M., 1998, Galactic Astronomy. Princeton Univ. Press, Princeton, NJ
Binney J., Gerhard O. E., Stark A. A., Bally J., Uchida K. I., 1991, MNRAS, 252, 210 (BGSBU)
Binney J., Gerhard O., Spergel D., 1997, MNRAS, 288, 365
Bissantz N., Englmaier P., Gerhard O., 2003, MNRAS, 340, 949
Blitz L., Spergel D. N., 1991, ApJ, 379, 631
Cole D. R., Debattista V. P., Erwin P., Earp S. W. F., Roškar R., 2014, MNRAS, 445, 3352
Combes F., 1996, in Buta R., Crocker D. A., Elmegreen B. G., eds, ASP Conf. Ser. Vol. 91, IAU Colloq. 157: Barred Galaxies. Astron. Soc. Pac., San Francisco, p. 286
Dame T. M., Thaddeus P., 2008, ApJ, 683, L143
Dwek E. et al., 1995, ApJ, 445, 716
Englmaier P., Gerhard O., 1997, MNRAS, 287, 57
Englmaier P., Gerhard O., 1999, MNRAS, 304, 512
Ferrière K. M., 2001, Rev. Mod. Phys., 73, 1031
Fux R., 1999, A&A, 345, 787
Hanawa T., Kikuchi D., 2012, in Pogorelov N. V., Font J. A., Audit E., Zank G. P., eds, ASP Conf. Ser. Vol. 459, Numerical Modelling of Space Plasma Slows (ASTRONUM 2011). Astron. Soc. Pac., San Francisco, p. 310
Jenkins A., Binney J., 1994, MNRAS, 270, 703
Kim W.-T., Seo W.-Y., Stone J. M., Yoon D., Teuben P. J., 2012a, ApJ, 747, 60
Kim W.-T., Seo W.-Y., Kim Y., 2012b, ApJ, 758, 14
Kim W.-T., Kim Y., Kim J.-G., 2014, ApJ, 789, 68
Lee C. W., Lee H. M., Ann H. B., Kwon K. H., 1999, ApJ, 513, 242
Maciejewski W., 2008, in Bureau M., Athanassoula E., Barbuy B., eds, Proc. IAU Symp. Vol. 245, Formation and Evolution of Galaxy Bulges. Kluwer, Dordrecht, p. 161
Mignone A., Bodo G., Massaglia S., Matsakos T., Tesileanu O., Zanni C., Ferrari A., 2007, ApJS, 170, 228
Mulder W. A., Liem B. T., 1986, A&A, 157, 148
Patsis P. A., Athanassoula E., 2000, A&A, 358, 45
Pettitt A. R., Dobbs C. L., Acreman D. M., Price D. J., 2014, MNRAS, 444, 919
Riemann G. F. B., 1860, Abh. Konigl. Gesell. Wiss. Göttingen., 43, 192
Rodriguez-Fernandez N. J., Combes F., 2008, A&A, 489, 115
Roe P. L., 1986, Annu. Rev. Fluid Mech., 18, 337
Sod G. A., 1978, J. Comput. Phys., 27, 1
Sofue Y., 2013, in Oswalt T. D., Gilmore G., eds, Planets, Stars and Stellar Systems, Vol. 5. Springer-Verlag, Dordrecht, p. 985
Sormani M. C., Magorrian J., 2015, MNRAS, 446, 4186
Stanek K. Z., Mateo M., Udalski A., Szymanski M., Kaluzny J., Kubiak M., 1994, ApJ, 429, L73
van Albada T. S., Sanders R. H., 1982, MNRAS, 201, 303
van Albada G. D., van Leer B., Roberts W. W., Jr, 1982, A&A, 108, 76
van Leer B., 1977, J. Comput. Phys., 23, 263
Wada K., Koda J., 2004, MNRAS, 349, 270
Weiner B. J., Sellwood J. A., 1999, ApJ, 524, 112

This paper has been typeset from a TEX/LATEX file prepared by the author.

Downloaded from https://academic.oup.com/mnras/article/449/3/2421/1121938 by CNRS - ISTO user on 26 April 2022